

# Sliding Mode Control of an Ultra High Speed Centrifugal Compressor for the Air Management of Fuel Cell Systems for Automotive Applications

Dongdong Zhao\*, Fei gao\*, *Member, IEEE*, David Bouquain\*, Manfeng Dou<sup>†</sup>, *Member, IEEE*, Abdellatif Miraoui\*, *Senior Member, IEEE*,

\* IRTES-SET Laboratory, University of Technology of Belfort-Montbéliard,  
90010 Belfort, France

Emails: (dongdong.zhao, fei.gao, david.bouquain, abdellatif.miraoui)@utbm.fr

<sup>†</sup> Institute of REPM Electrical Machines and Control Technology, Northwestern Polytechnical University, 710072 Xi'an, China

Email: doumf@nwpu.edu.cn

## Abstract

This paper presents the modeling and control of an ultra high speed centrifugal compressor for the air management of proton exchange membrane fuel cell (PEMFC) systems. Centrifugal compressors have advantages of compactness, high efficiency, as well as low noise compared with other kinds of displacement compressors. Moreover, the ultra high speed technology can also reduce the size and weight of the compressor, which makes it feasible for automotive applications. However, the adoption of a centrifugal compressor results in the difficulty of control because of the coupling between mass flow and pressure. In this paper, a neural network model of the compressor is developed and a decentralized sliding mode controller based on twisting and super twisting algorithms is proposed and tested to control the compressor pressure and mass flow. The experimental results show good dynamic characteristics and faster response compared with conventional PI control.

## NOMENCLATURE

$\chi_{O_2}$  Oxygen molar fraction in the air

$\eta_{cp}$	Compressor efficiency
$\gamma$	Thermal ratio coefficient of the air
$\lambda_{O_2}$	Oxygen excess ratio
$\omega$	Compressor rotational speed (in radians per second)
$\phi_{atm}$	Relative humidity of the air
$\Psi_f$	PM rotor flux linkage (in Webber)
$\theta$	Control valve position (in radian)
$C_p$	Specific heat capacity of the air (in J/(mol·K))
$E_{oc}$	Fuel cell single cell open circuit voltage (in volt)
$F$	Faraday number (in coulombs)
$i$	Fuel cell stack current density (in amperes per square meters)
$i_d, i_q$	d,q components of the stator winding current (in ampere)
$I_{st}$	Stack current (in ampere)
$L_d, L_q$	d,q axis inductances of the motor (in Henry)
$m$	Air mass accumulated in the manifold (in kilogram)
$M_{air}$	molar mass of atmospheric air (in kg/mol)
$M_{O_2}$	molar mass of oxygen (in kg/mol)
$N_{cell}$	Number of cells
$p$	Manifold air pressure (in atm)
$p_{atm}$	Atmosphere pressure (in atm)
$p_{H_2}$	Partial pressure of hydrogen (in atm)
$P_{motor}$	Number of pole pairs of the motor
$p_{O_2}$	Partial pressure of oxygen (in atm)
$P_{st}$	Fuel cell output power (in watt)
$q$	Compressor air flow rate (in kilogram per second)
$q_{out}$	Air mass flow rate out of the manifold (in kilogram per second)
$R$	Universal gas constant (in J/(mol·K))
$R_a$	Air gas constant taking into consideration of the heat ratio (in J/(kg·K))
$S_{tot}$	Fuel cell total active surface area (in square meters)
$T$	The temperature of the air in the manifold (in Kelvin)
$T_{cm}$	Electromagnetic torque of the motor (in N·m)
$T_{cp}$	Compressor torque (in N·m)

$T_{fc}$	Fuel cell stack temperature (in Kelvin)
$V$	Manifold volume (in cubic meter)
$V_{act}$	Fuel cell single cell activation losses (in volt)
$V_{cell}$	Fuel cell single cell voltage (in volt)
$V_{ohmic}$	Fuel cell single cell ohmic losses (in volt)
$V_{stack}$	Fuel cell stack output voltage (in volt)
$V_{trans}$	Fuel cell single cell transport losses (in volt)
$W_{ca,in}$	Inlet air mass flow rate (in kilogram per second)
$W_{o_2,in}$	Inlet oxygen mass flow rate (in kilogram per second)
$W_{o_2,reacted}$	Oxygen reaction rate (in kilogram per second)

## I. INTRODUCTION

Thanks to its low temperature working condition (40 °C-180 °C), the proton exchange membrane fuel cell (PEMFC) allows a faster system start up than those fuel cells (such as MCFC and SOFC) using high temperature technologies, which makes it most suitable for automotive applications [1]. Two different kinds of PEMFC, low temperature PEMFC (40 °C-90 °C) and high temperature PEMFC (120 °C-180 °C), have been studied for automotive applications over the past few years [2]–[7]. **For fuel cell electrical vehicles, the power demand from the fuel cell relates much to the energy management strategy [8]–[12]. A simple control method can be used if the power demand is constant. Whereas, if varied power is drawn from the fuel cell a fast and accurate controller should be developed to improve the fuel cell dynamic response.** In the fuel cell controller development, the management of air supplied to the fuel cell cathode is one of the key factors [13]. In order to achieve desired fuel cell operating conditions, the air supplied to the cathode needs to be compressed. The air compressor which consumes up to 30 % of fuel cell generated power in the worst cases is a crucial component in the air management system. Therefore, the power volume and efficiency of the compressor directly influence the overall system efficiency [14].

A scroll compressor driven by an induction motor is employed in [1], [15], [16]. A twin-screw compressor is used for the high-pressure condition and a blower is used for the low-pressure condition in [17]. Screw or roots-type superchargers mentioned in the above literatures are commonly chosen for their easier technical implementations. The centrifugal compressor has major advantages of compactness, low-noise, and high efficiency, which is more suitable for automotive applications. However, it is more difficult to be implemented in terms of control [15], [18]. Among different control strategies, sliding mode control

shows interests of good robustness and easy application, etc. Air management of fuel cell systems based on sliding mode control has been presented in [19]–[22]. In these references, the system is modeled as one input (compressor input voltage) system and the only control objective is the oxygen excess ratio. However, pressure ratio, which relates to system efficiency and security, is also a crucial performance parameter. In this paper, the pressure ratio is considered as another control objective besides oxygen excess ratio. The main contributions of this article are as follows:

- 1) A neural network model of the ultra high speed centrifugal compressor is developed and analyzed. To the best of our knowledge, this is the first reported experimental test of an ultra high speed centrifugal compressor for the air management of fuel cell systems.
- 2) A fast butterfly valve is employed and the valve angle is considered as one of the sliding control variables. In this way, the system becomes a two inputs (valve angle and electromagnetic torque of the compressor) system, which makes it possible to control the mass flow and pressure simultaneously.
- 3) Two decentralized sliding mode algorithms (twisting and super twisting) are developed to control the pressure and mass flow respectively. The appropriate control parameter design ensures the convergence and stability of the control system.

This paper is organized as follows. Section II gives a general description of the air management in fuel cell systems and requirements to the air management system for automotive applications are presented. In section III, a mathematical model of the air management system based on a ultra high speed centrifugal compressor is developed. In section IV, a decentralized sliding mode controller is designed to control the mass flow and pressure. The experimental setup and validation are given in section V and VI respectively.

## II. AIR MANAGEMENT OF PEMFCs FOR AUTOMOTIVE APPLICATIONS

### A. Air management descriptions

A fuel cell requires constant supply of clean air to be delivered at a proper pressure in order to function effectively [23]. In [5], the air flow circuit not only supplies sufficient reactants but also serves as a cooling device. Moreover, in automotive applications, due to the dynamic load characteristic, the flow rate of the air has to be regulated as the operating point changes. Thus, an air management system is needed to provide sufficient air flow for the fuel cell and regulate the pressure at the same time to make fuel cell work at its optimal efficiency. Different kinds of equipments (see Fig. 1) are needed to fulfill these tasks. Explicit descriptions of the air management system and the tasks of each component

are presented in [1]. The requirements to the air management systems for automotive applications are described in the following section.

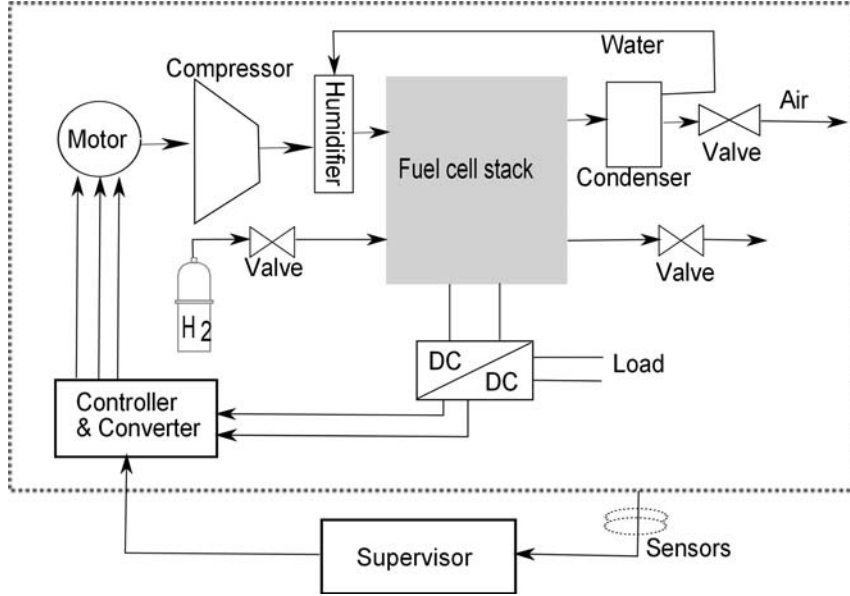


Fig. 1. Air management system.

### B. Requirements for automotive applications

1) *Compactness*: Two of the main drawbacks of current air compressors in fuel cell systems for automotive application are their large size and considerable weight. It is well known that compared with other displacement compressors, centrifugal compressors have the advantages of compactness and high efficiency. Comprehensive comparisons between centrifugal compressor and positive displacement compressors (scroll compressor, lobe compressor, screw compressor, etc.) have been published previously [1]. The adoption of ultra high speed technology in the compressor design results in the ultra compactness. The major advantage of high rotational speed is the decrease of the impeller radius and therefore an increase in power density in turbo machinery. Also the electrical motor power density is roughly proportional to the speed [24]. The design of the compressor used in this paper is presented in [25], which is based on a similar small high-speed compressor data in [24].

2) *Oxygen excess ratio control*: Oxygen excess ratio  $\lambda_{O_2}$  is define as the ratio between the oxygen  $q_{O_2,in}$  entering the cathode and the oxygen  $q_{O_2,reacted}$  consumed due to the electrochemical reac-

tion [26]–[28]:

$$\lambda_{o_2} = \frac{q_{o_2,in}}{q_{o_2,reacted}} \quad (1)$$

$\lambda_{o_2}$  is considered as a performance variable of the system and its control is an important factor since it ensures the safety of the fuel cell [27]. The small value of  $\lambda_{o_2}$  leads to the starvation phenomenon of the fuel cell stack [26], which degrades fuel cell performance and shortens the stack life time. A large value of  $\lambda_{o_2}$  results in excessive parasitic power consumption, therefore, a lower efficiency. The optimal value of  $\lambda_{o_2}$ , which depends heavily on the fuel cell operating conditions (current, temperature, water content, etc.), needs to be determined [29] [30]. However, this paper does not focus on the determination of this value. In this paper, the value of 2, which contains some security margin and provides a good performance [13], [14], [26], is adopted for the validation of the controller.

3) *pressure control*: For the fuel cell stack, large pressure ripples may damage the membrane and produce voltage pulsation, which should be avoided. Keeping the pressure at a constant can effectively protect the stack membrane from damage. However, unlike displacement compressors, pressure control is challenging for centrifugal compressor as the mass flow and pressure control are strongly coupled [1], [15], [18]. During the fuel cell operation, the mass flow has to be promptly regulated according to the load situation. Meanwhile the pressure has to be control in time, otherwise it may be varied greatly. In severe cases, the pressure may be dragged out of the normal operating region, which will paralyze the whole system. Moreover, the highly nonlinear characteristic of mass flow, pressure, and speed also adds difficulty to the pressure control.

4) *surge control*: Surge is defined as the operating point at which the compressor peak head capability and minimum flow limit are reached. The compressor loses the ability to maintain the peak head when surge occurs and the entire system becomes unstable [31]. Surge is an unstable state, which gives rise to oscillations of mass flow and pressure ratio, and severely reduces compressor efficiency. Moreover, it can possibly damage the compressor in the most severe cases [32]. An effective and direct way to deal with the surge constraint is to make the compressor operate to the right of the surge line which is defined experimentally.

In our previous works, the requirement of compactness has been fulfilled by designing an ultra high speed centrifugal compressor [25]. Meanwhile the surge control is realized by a reference limiter [33]. This paper focuses on the oxygen excess ratio and pressure control via decentralized sliding mode control method.

### III. SYSTEM MODELING

#### A. Fuel cell stack modeling

The comprehensive fuel cell stack model reported in [34] is adopted for the validation of the control methodology. The mass flow rate of oxygen consumed in the cathode  $q_{O_2,reacted}$  is calculated as follows:

$$q_{O_2,reacted} = M_{O_2} \frac{N_{cell} I_{st}}{4F} \quad (2)$$

The inlet cathode mass flow rate of oxygen  $q_{O_2,in}$ :

$$q_{O_2,in} = \chi_{O_2} \cdot q_{ca,in} \quad (3)$$

where  $\chi_{O_2}$  is the oxygen molar fraction in the air. According to (1),(2),(3), and taking into account the relative humidity of the air  $\phi_{atm}$ , the final expression of the air mass flow reference  $q^*$  results [19]:

$$q^* = (1 + \phi_{atm}) \frac{1}{\chi_{O_2}} \lambda_{O_2,ref} M_{O_2} \frac{n I_{st}}{4F} \quad (4)$$

The stack output voltage  $V_{stack}$  is modeled from a single-cell static characteristic [15], [23], [34]:

$$V_{stack} = (E_{oc} - V_{ohmic} - V_{act} - V_{trans}) \times N_{cell} \quad (5)$$

where  $N_{cell}$  is the number of cells.  $E_{oc}$  is the open circuit voltage which relates to the partial pressures of hydrogen and oxygen inside the stack [15], [23], [34]. **The structure of the fuel cell stack voltage model is shown in Fig. 2. In this model we assume other subsystems, such as humidifier, cooling system, etc are appropriately controlled.**

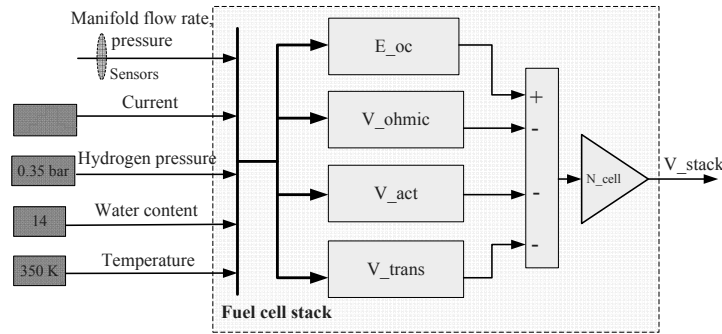


Fig. 2. Diagram of the fuel cell model.

$$E_{oc} = 1.229 - 0.85 \times 10^{-3}(T_{fc} - 298.15) + 4.3085 \times 10^{-5} \\ * T_{fc} * [\ln(p_{H_2}) + 0.5 \ln(p_{O_2})] \quad (6)$$

where  $T_{fc}$  is the temperature of the stack expressed in Kelvin.  $p_{H_2}$  and  $p_{O_2}$  are the partial pressures of hydrogen and oxygen respectively.

Denote current density by  $i$ . Then, ohmic losses  $V_{ohmic}$ , activation losses  $V_{act}$  and transport losses  $V_{trans}$  are explained as follows [34]–[39]:

- 1)  $V_{ohmic} = i r$  is due to the electrical resistance of the electrodes, and the resistance to the flow of ions in the electrolyte.  $r$  represents the fuel cell internal electrical resistance [40].
- 2)  $V_{act} = A \ln\left(\frac{i}{i_0}\right)$  is due to the electrochemical irreversible reactions. Both  $A$  and  $i_0$  are constants, which can be determined empirically.
- 3)  $V_{trans} = m \exp(n i)$  results from the variation of the reactant concentration at fuel cell catalyst interface as the fuel is consumed.  $m$  and  $n$  are constants that depend on the temperature and the reactant partial pressure and can be determined empirically.

The relation of the current density  $i$  (A/m<sup>2</sup>), the stack current  $I_{st}$  (A), the number of cells  $N_{cell}$ , and the total active surface area  $S_{tot}$  (m<sup>2</sup>) is given by [15]:

$$i = \frac{I_{st} N_{cell}}{S_{tot}} \quad (7)$$

Thus, the fuel cell power is calculated as follows:

$$P_{st} = I_{st} \cdot V_{stack} = N_{cell} \cdot V_{cell} \cdot I_{st} \quad (8)$$

where  $V_{cell}$  is the single cell voltage.

### B. Compressor modeling

The manufactured compressor prototype (Fig. 3) has a weight of 0.6 kg which is fifty times lower than a comparable scroll compressor. This compressor has been evaluated and characterized on a test bench. The measured compressor efficiency at its rated operating point (250,000 rpm, 13 g/s, pressure ratio of 1.4 atm (**1 atm=101.325 kPa**), inlet temperature 300 K) is 74.8 %. The motor efficiency at the rated operating point is 92 %. The experimental compressor map is shown in Fig. 5(a). Fig. 5(b) gives the compressor power map. In order to find out the mathematical relation of mass flow, pressure ratio and compressor speed, a neural network based on the back propagation (BP) algorithm is trained off line on the basis of the experimental data. The structure of the developed neural network is shown in Fig. 4. Fig. 5(a) shows that the trained neural network model has a very good agreement with the experimental data. Therefore, the compressor model based on neural network can be expressed as follows:

$$q = h(\omega, p) \quad (9)$$



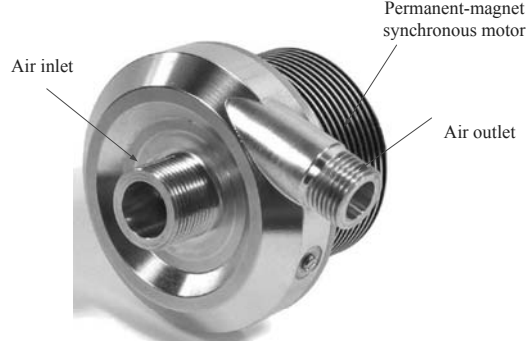


Fig. 3. Realized compressor prototype.

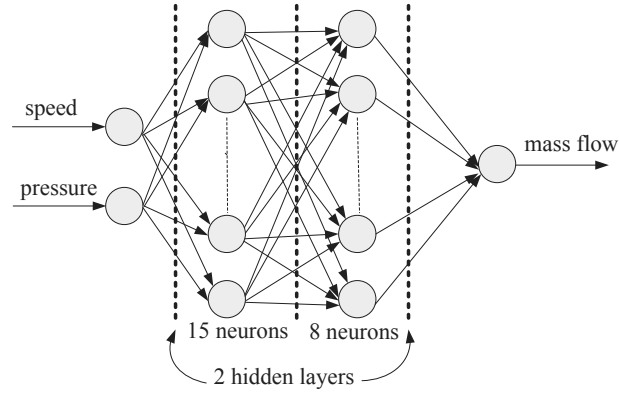


Fig. 4. Developed centrifugal compressor model.

where  $q$ ,  $\omega$ ,  $p$  are the compressor mass flow rate, angular velocity and pressure ratio respectively. The equations used in this model are detailed as follows:

The output of the neural network:

$$q = \text{purelin}(w_1\beta_1 + w_2\beta_2 \cdots w_8\beta_8 + d) \quad (10)$$

2nd hidden layer outputs:

$$\beta_j = \text{purelin}(l_{1,j}\alpha_1 + l_{2,j}\alpha_2 \cdots l_{15,j}\alpha_{15} + e_j), j = 1, 2 \cdots, 8 \quad (11)$$

1st hidden layer outputs:

$$\alpha_i = \text{tansig}(a_i p + b_i \omega + c_i), i = 1, 2 \cdots, 15 \quad (12)$$

where  $w_j, l_{i,j}, a_i, b_i$  are the weight coefficients.  $d, e_j, c_i$  are the biases.  $\text{purelin}(\cdot)$  and  $\text{tansig}(\cdot)$  are linear transfer function and hyperbolic tangent sigmoid transfer function respectively. The mathematical

expressions of these two functions are  $purelin(x) = x$  and  $tansig(x) = \frac{2}{1+e^{-2x}} - 1$  respectively. Summarizing (10)(11)(12), the final expression of  $q$  can be expressed as a function of  $\omega$  and  $p$ :

$$q = h(\omega, p) = w_1(l_{1,1}\alpha_1 + l_{2,1}\alpha_2 \cdots l_{15,1}\alpha_{15} + e_1) + w_2(l_{1,2}\alpha_1 + l_{2,2}\alpha_2 \cdots l_{15,2}\alpha_{15} + e_2) + \cdots + w_8(l_{1,8}\alpha_1 + l_{2,8}\alpha_2 \cdots l_{15,8}\alpha_{15} + e_8) + d \quad (13)$$

where

$$\alpha_i = \frac{2}{1 + e^{-2(a_i p + b_i \omega + c_i)}} - 1, i = 1, 2, \dots, 15. \quad (14)$$

In (13)(14), 182 parameters exist, which are obtained by the BP training algorithm. The parameters of the model are shown in the appendix, TABLE III.

### C. Air supply manifold

The manifold represents the lumped volume of the pipes between the compressor and the fuel cell stack. The dynamics of the air pressure in the manifolds directly relates to the compressor characteristic. According to the mass conservation principle, the dynamics of the air mass  $m$  accumulated in the manifold volume and air pressure  $p$  can be expressed by following equations [34], [41], [42]:

$$\frac{dm}{dt} = q - q_{out} \quad (15)$$

$$\frac{dp}{dt} = \frac{\gamma R}{M_{air} V} (q T_{in} - q_{out} T_{out}) \quad (16)$$

where  $q_{out}$  is the air mass flow out of the manifold.  $T_{in}, T_{out}$  are temperatures of the gas into and out of the manifold respectively.  $M_{air} = 0.029 \text{ kg/mol}$  is the molar mass of atmospheric air.  $\gamma = 1.4$  is the thermal ratio coefficient of the air and  $R = 8.31 \text{ J/(mol}\cdot\text{K)}$  is the universal gas constant.  $V$  is the manifold volume. In this paper, the air temperature in the manifold is assumed to be constant. That is  $T_{in} = T_{out} = T$ . Then, (16) can be expressed as follows:

$$\frac{dp}{dt} = \frac{R_a T}{V} (q - q_{out}) \quad (17)$$

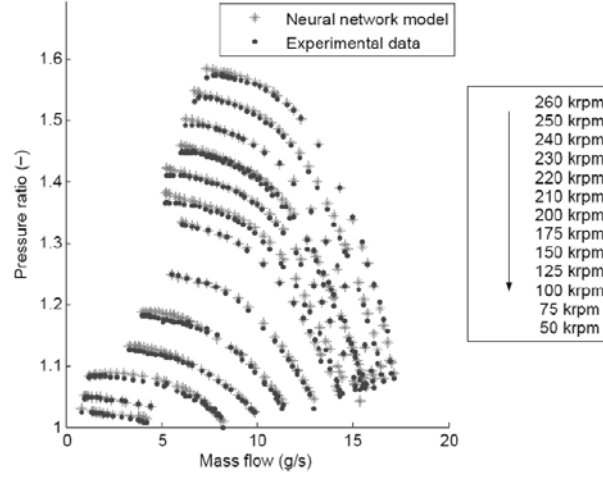
where  $R_a = \gamma * R / M_{air}$  is the air gas constant taking into consideration of the heat ratio.

General nozzle flow equations are used to calculate  $q_{out}$ , which is divided into two regions by the critical pressure ratio  $\xi$ .

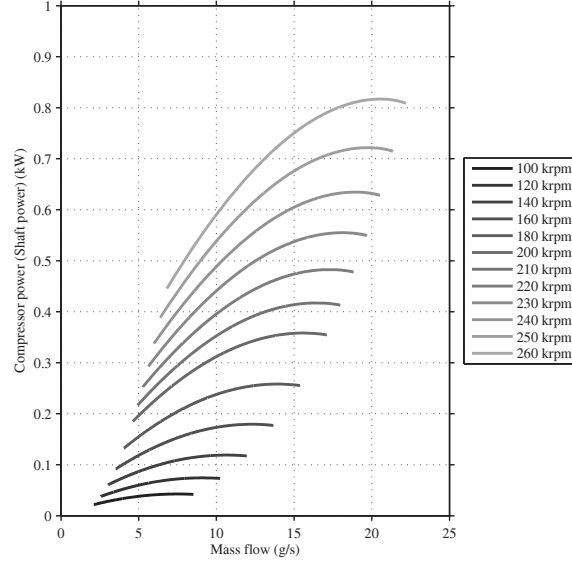
$$\xi = \left( \frac{p_{atm}}{p} \right)_{crit} = \left( \frac{2}{\gamma + 1} \right)^{\frac{\gamma}{\gamma - 1}} \quad (18)$$

For  $\frac{p_{atm}}{p} > \xi$ ,

$$q_{out} = C_d p S_{ctrl}(\theta) \sqrt{\frac{2\gamma M_{air}}{(\gamma - 1)RT} \left[ \left( \frac{p_{atm}}{p} \right)^{\frac{2}{\gamma}} - \left( \frac{p_{atm}}{p} \right)^{\frac{\gamma+1}{\gamma}} \right]} \quad (19)$$



(a) Measured compressor map and neural network model map.



(b) Calculated power map of the compressor.

Fig. 5. Compressor map and power map.

For  $\frac{p_{atm}}{p} \leq \xi$ ,

$$q_{out} = C_d p S_{ctrl}(\theta) \sqrt{\frac{\gamma M_{air}}{RT} \left( \frac{2}{\gamma - 1} \right)^{\frac{1+\gamma}{1-\gamma}}} \quad (20)$$

where  $\theta$ ,  $p_{atm}$  are the open angle of valve, atmosphere pressure respectively.  $C_d$  is the discharge coefficient

of the Nozzle.  $S_{ctrl}(\theta)$  is the open area of the valve:

$$S_{ctrl}(\theta) = \pi \cdot r_v^2 \cdot \theta \quad (21)$$

where  $r_v$  is the radius of the valve.

The critical pressure ratio  $\xi$  is equal to 0.528. In our test conditions, the pressure  $p$  is below 1.6 atm . Assuming  $p_{atm} = 1$  atm, gives  $\frac{p_{atm}}{p} > 1/1.6 > 0.528$ . Therefore, only (19) is used for the mathematical model development.

#### D. Actuators modeling

The compressor is driven by a field-oriented controlled (FOC) permanent magnet synchronous motor (PMSM). The following equations show the dynamic property of the compressor angular velocity  $\omega$ :

$$\frac{d\omega}{dt} = \frac{1}{J}(T_{cm} - T_{cp}) \quad (22)$$

where  $J$  is the moment of inertia.  $T_{cm}$  is the electromagnetic torque produced by the PMSM.  $T_{cp}$  is the compressor torque which is deemed as load torque. They can be expressed as follows:

$$T_{cm} = \frac{3}{2}P [\Psi_f i_q + (L_d - L_q) i_d i_q] \quad (23)$$

$$T_{cp} = \frac{C_p}{\omega} \frac{T}{\eta_{cp}} \left[ \left( \frac{p}{p_{atm}} \right)^{\frac{\gamma-1}{\gamma}} - 1 \right] \cdot q \quad (24)$$

$i_d = 0$  control methodology is adopted. Thus (23) can be replaced by the following equation:

$$T_{cm} = \frac{3}{2}P \Psi_f i_q \quad (25)$$

where  $P$  is the number of pole pairs.  $\Psi_f$  is the PM rotor flux linkage.  $i_d, i_q$  are the d, q components of the stator winding current.  $L_d, L_q$  are d, q axis inductances.  $C_p$  is the specific heat capacity of the air.  $\eta_{cp}$  is the compressor efficiency. The parameters of the PMSM have been shown in TABLE I.

In the system, a fast butterfly valve is implemented to control the pressure ratio. A PI controller is designed to control the valve position. The valve position  $\theta$  is proportional to the current  $i_{vl}$  flowing through the converter,  $\theta \propto i_{vl}$ . As the valve has a much smaller inertia than the compressor, its response time ( $t_{vl} < 0.1s$ ) can be neglected. In this case, the valve position  $\theta$  can be deemed as input directly instead of  $i_{vl}$ .

TABLE I  
SPECIFICATIONS OF THE PMSM

Number of pole pairs	1
Moment of inertia	$5.5 \times 10^{-7}$ kg· m <sup>2</sup>
Magnet flux linkage	$6 \times 10^{-3}$ Wb
max power	900 W
max torque	34 mNm
max frequency	4.33 kHz
Stator resistance	0.9 $\Omega$
Stator inductance	160 $\mu$ H

#### IV. DECENTRALIZED SLIDING MODEL CONTROLLER DESIGN

From above mathematical models, the state space equations of the air management can be formulated as follows:

$$\dot{p} = \frac{R_a T}{V} (h(x) - \varphi(x, \theta)) = f_1(x) + g_1(x) \cdot \theta \quad (26)$$

$$\dot{\omega} = f_2(x) + g_2(x) \cdot i_q \quad (27)$$

$$q = h(x) \quad (28)$$

where  $x = [\omega, p]$ .  $\varphi(x, \theta)$  is the outlet flow rate which can be obtained by (19).  $f_1(x), g_1(x), f_2(x), g_2(x)$  are expressed as follows:

$$f_1(x) = \frac{R_a T}{V} h(x) \quad (29)$$

$$g_1(x) = -\frac{R_a T}{V} C_d p \pi r_v^2 \sqrt{\frac{2\gamma M_{air}}{(\gamma-1)RT} \left[ \left( \frac{p_{atm}}{p} \right)^{\frac{2}{\gamma}} - \left( \frac{p_{atm}}{p} \right)^{\frac{\gamma+1}{\gamma}} \right]} \quad (30)$$

$$f_2(x) = \frac{-C_p T_{atm}}{J\omega \eta_{cp}} \left[ \left( \frac{p}{p_{atm}} \right)^{\frac{\gamma-1}{\gamma}} - 1 \right] \cdot h(x) \quad (31)$$

$$g_2(x) = \frac{3}{2J} P \Psi_f \quad (32)$$

The main control objective is to make the mass flow and pressure follow given references. The control variables are  $u_1 = \theta$  and  $u_2 = i_q$ . This system is input-output coupled. Corresponding coupling degree has been analyzed in [43] using RGA method. According to the analysis, decentralized control can be used to control mass flow and pressure separately. Mass flow is controlled by compressor speed which is driven by  $i_q$ , and pressure ratio is controlled by valve angle  $\theta$ . In this paper, a decentralized sliding

mode controller based on twisting and super twisting algorithms is designed. The sliding surfaces are defined as follows:

$$s_1 = p^* - p \quad (33)$$

$$s_2 = q - q^* \quad (34)$$

$q^*$  and  $p^*$  are the references of mass flow and pressure ratio respectively.  $p^*$  is kept at a constant 1.4 bar, on the basis of the fuel cell stack requirement.  $q^*$  is calculated online by the equation (4) according to the power demand, supposing  $\lambda_{o_2,ref} = 2$ .

Differentials of the sliding variables  $s_1$  and  $s_2$  are expressed as follows:

$$\begin{aligned} \dot{s}_1 &= \dot{p}^* - \dot{p} \\ &= -f_1(x) - g_1(x) \cdot \theta \end{aligned} \quad (35)$$

$$\begin{aligned} \dot{s}_2 &= \dot{q} - \dot{q}^* \\ &= H_p(x)(f_1(x) + g_1(x) \cdot \theta) + H_\omega(x)(f_2(x) + g_2(x) \cdot i_q) - \dot{q}^* \end{aligned} \quad (36)$$

where  $H_\omega(x) = \frac{\partial h}{\partial \omega}$  and  $H_p(x) = \frac{\partial h}{\partial p}$ . In this case, the system relative degree is one,  $r_j = 1, (j = 1, 2)$ , because the control variables explicitly appear in (35),(36). Considering the convergence and stability of the system, twisting control algorithm is used for pressure control, and super twisting algorithm is employed for mass flow control. The derivation of  $\theta$  is bounded as the result of the twisting control algorithm, which provides a essential condition for the convergency of the mass flow control based on the super twisting algorithm. In this case, the stability and convergency of the system can be guaranteed by selecting the appropriate control parameters. For the entire system, some bounds of the variables are shown in TABLE II.

TABLE II  
PARAMETER RANGE

Parameters	bounds	unit
Manifold pressure: $p$	[1 1.6]	atm
Compressor rotational speed: $\omega$	[0 8670 $\pi$ ]	rad/s
Mass flow rate: $q$	[0 16 * 10 <sup>-3</sup> ]	kg/s
Valve open angle: $\theta$	[0.01 $\pi$ 0.5 $\pi$ ]	rad
q-axis current: $i_q$	[0 10]	A

Details of the controller design are described in the following subsections.

#### A. Pressure control

The 2nd order differential of the sliding variable  $s_1$  can be expressed as follows:

$$\begin{aligned}\ddot{s}_1 &= \frac{\partial \dot{s}_1}{\partial p} \dot{p} + \frac{\partial \dot{s}_1}{\partial \omega} \dot{\omega} + \frac{\partial \dot{s}_1}{\partial u_1} \dot{u}_1 \\ &= \varphi_1(p, \theta, \omega, i_q) - g_1(p, \omega) \dot{u}_1\end{aligned}\quad (37)$$

Depending on the bounds of the state variables and control variables shown in TABLE II, the following conservative ranges are determined:

$$|\varphi_1(\cdot)| \leq \Phi, 0 < \Gamma_m \leq -g_1(\cdot) \leq \Gamma_M \quad (38)$$

where  $\Phi = 0.3, \Gamma_m = 0.35, \Gamma_M = 0.7$ . Twisting control algorithm [44]:

$$\dot{\theta} = \begin{cases} -V_m \text{sign}(s_1), & \text{if } s_1 \dot{s}_1 \leq 0 \\ -V_M \text{sign}(s_1), & \text{if } s_1 \dot{s}_1 > 0 \end{cases} \quad (39)$$

The corresponding sufficient conditions for the finite time convergence to the sliding manifold are [44]:

$$V_M > V_m \quad (40)$$

$$V_m > \frac{4\Gamma_M}{r_0} \quad (41)$$

$$V_m > \frac{\Phi}{\Gamma_m} \quad (42)$$

$$\Gamma_m V_M - \Phi > \Gamma_M V_m + \Phi \quad (43)$$

where  $r_0$  is a positive constant, which defines the convergence domain of the twisting control. In our calculation  $r_0$  is set equal to 1. Based on these conditions, the control parameters are selected as follows:  $V_M = 10, V_m = 3$ . The following differentiator [22] [45] is used to obtain the derivation of  $s_1$ .

$$\dot{z}_0 = -\sigma_1 L^{\frac{1}{2}} |z_0 - s_1|^{\frac{1}{2}} \text{sign}(z_0 - s_1) + z_1 \quad (44)$$

$$\dot{z}_1 = -\sigma_2 L \text{sign}(z_1 - \dot{z}_0) \quad (45)$$

where  $z_0$  and  $z_1$  are the online estimations of  $s_1$  and  $\dot{s}_1$  respectively. The parameters of the differentiator are chosen empirically as follows:  $\sigma_1 = 1.5, \sigma_2 = 1.1, L = 4$ .

### B. Mass flow control

The 2nd order differential of the sliding variable  $s_2$  can be expressed as follows:

$$\begin{aligned}\ddot{s}_2 &= \frac{\partial \dot{s}_2}{\partial p} \dot{p} + \frac{\partial \dot{s}_2}{\partial \theta} \dot{\theta} + \frac{\partial \dot{s}_2}{\partial \omega} \dot{\omega} + \frac{\partial \dot{s}_2}{\partial u_2} \dot{u}_2 - \ddot{q}^* \\ &= \varphi_2(p, \theta, \omega, i_q, \dot{\theta}, \ddot{q}^*) + \gamma_2 \dot{u}_2\end{aligned}\quad (46)$$

Equation (46) shows that the boundary of  $\varphi_2$  not only depends on the state variables and control variables but also relates to the derivation of  $\theta$ . Thus, it is necessary to limit the value of  $\dot{\theta}$ . From (39), the twisting control algorithm results  $|\dot{\theta}| \leq V_M$ . Under such circumstances, the following inequality will hold:

$$|\varphi_2(\cdot)| \leq C \quad (47)$$

$$0 < L_m \leq \gamma_2 \leq L_M \quad (48)$$

According to super twisting control algorithm [44] [19], the control variable  $u_2$  can be expressed as follows:

$$u_2 = \nu_1 + \nu_2 \quad (49)$$

$$\dot{\nu}_1 = -\eta \text{sign}(s_2) \quad (50)$$

$$\nu_2 = \begin{cases} -\lambda |s_0|^{\frac{1}{2}} \text{sign}(s_2), & \text{if } |s_2| > |s_0| \\ -\lambda |s_2|^{\frac{1}{2}} \text{sign}(s_2), & \text{if } |s_2| \leq |s_0| \end{cases} \quad (51)$$

$s_0$  is set to 0.001. The conditions for the convergence are given by the following inequalities:

$$\eta > \frac{C}{L_m} \quad (52)$$

$$\lambda^2 \geq \frac{4CL_M(\eta + C)}{L_m^3(\eta - C)} \quad (53)$$

It should be noted that the expression of  $\varphi_2(\cdot)$  is too complicated to be calculated because of the complexity of the compressor neural network model. In this paper, the value of  $C$  is not actually obtained. Therefore, the control parameters  $\eta$  and  $\lambda$  are identified empirically and validated by experimental trials. The control parameters are settled ultimately as follows:  $\eta = 12, \lambda = 45$ .

## V. TEST BENCH SETUP

An hardware-in-the-loop (HIL) experimental setup (Fig. 6), which is divided into two parts (hardware and dSPACE software), has been devised for the assessment of the control methodology. The hardware is comprised of a centrifugal compressor, supply manifold, outlet manifold, valves, real time controllers, sensors, etc. The temperature, mass flow and pressure sensors are installed on the supply manifold. A fast



butterfly valve is set at the outlet point for the pressure control. The ultra compact centrifugal compressor introduced in section III has a maximum speed of 260,000 rpm.

A high-performance PMSM FOC algorithm is implemented by software on a DSP (TMS320F28334) at a current sampling frequency of  $f_c = 80$  kHz. Both a 13kW fuel cell stack model and the sliding mode controller are implemented in dSPACE (DS1104). **For dSPACE, both its sampling frequency and the switching frequency of its output PWM signal are set at 10 kHz.** The simulated maximum fuel cell stack current is 110 A and the number of cells is 200. The block diagram of this HIL testbench is shown in Fig. 7.

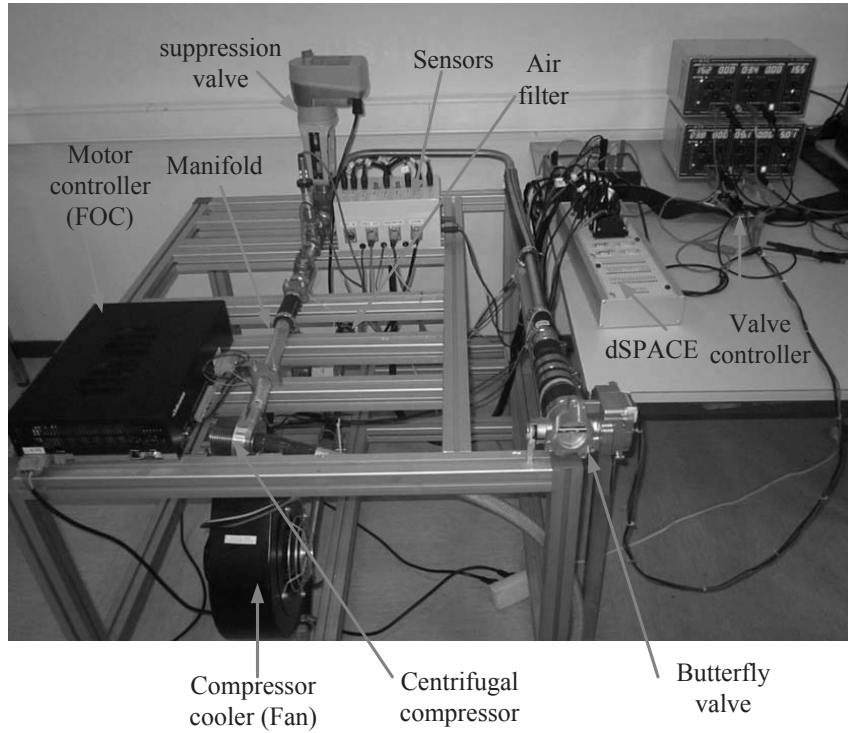


Fig. 6. Hardware-in-the-loop air management test bench.

## VI. MEASUREMENTS

On the basis of the stack requirement, the inlet manifold pressure reference is fixed at 1.4 bar. In the experiment, the current drawn from the stack is performed as depicted in Fig. 8. The following performance variables are used to judge the effectiveness the proposed controller:

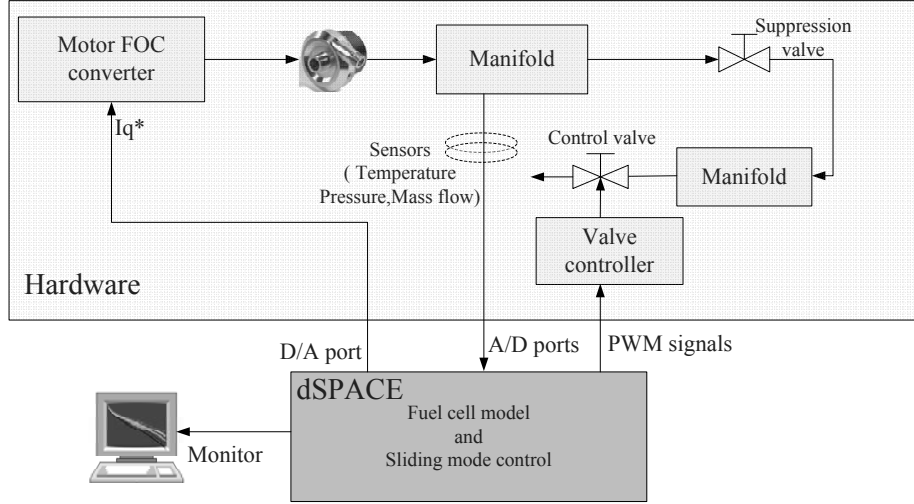


Fig. 7. Connections of the Hardware-in-the-loop test bench.

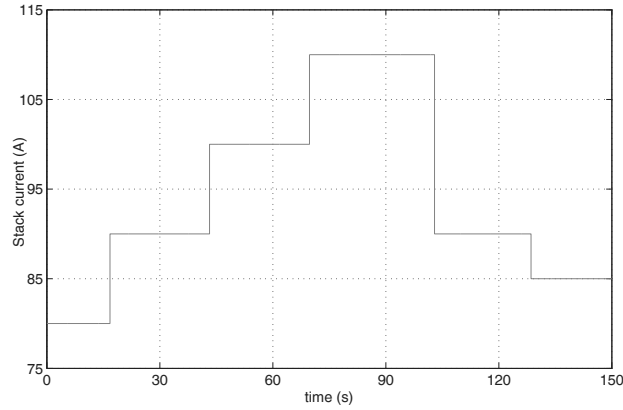


Fig. 8. Current drawn from the fuel cell stack.

1) *Oxygen excess ratio*: As depicted in II-B, oxygen excess ratio is a crucial variable which directly concern with the efficiency and security of the fuel cell stack. In this paper, an optimized value,  $\lambda_{o_2} = 2$ , is determined as one of the control targets. Under different load demands, the dynamic behavior of the oxygen excess ratio is depicted in Fig. 9. The deviations (at 20s, 45s, 70s, 100s, 130s) are caused by the abruptly current changes drawn from the stank. Fig. 10 gives a zoomed view of the oxygen excess ratio deviation shown in the pane of Fig. 9, which indicates that  $\lambda_{o_2}$  has a rapid recover time,  $t = 3$  s.

The quick recovery of  $\lambda_{o_2}$  results from the fast response of the mass flow, therefore, declines the

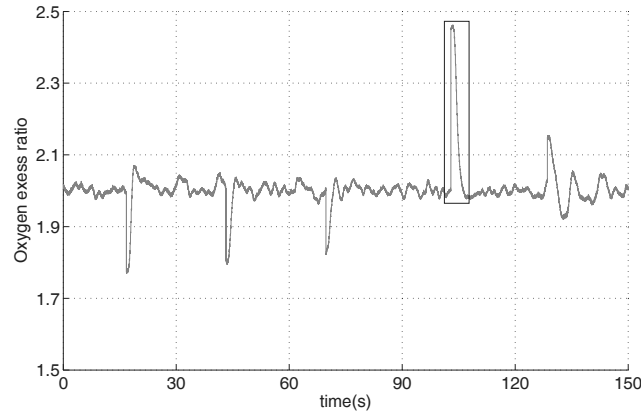


Fig. 9. Oxygen excess ratio.

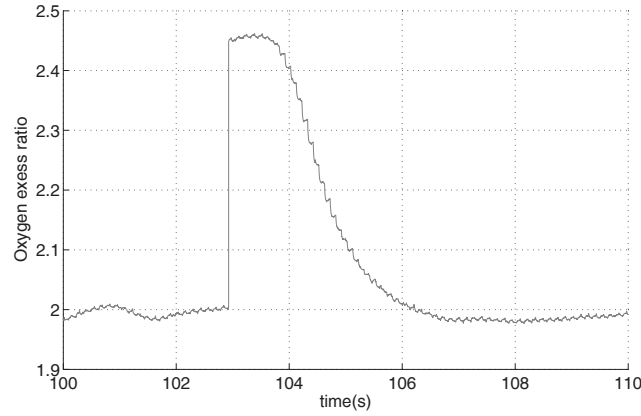


Fig. 10. Zoom of the deviation of oxygen excess ratio shown in Fig. 9.

oxygen starvation caused by the abruptly current increase drawn from the fuel cell stack. Both the small inertia of the compressor and appropriate control parameter configuration contribute to the fast respond of the mass flow. The mass flow dynamic during the operation is depicted in Fig. 11. Following a step load from 80 A to 90 A, corresponding mass flow from 11.3 g/s to 13.0 g/s, the response time is less than 1.5s, which is smaller than that of a conventional PI control (Fig. 12),  $t = 2.5$ s. The oscillations in Fig. 12 between 2s-4s is due to the reference limiter, which is developed for the prevention of compressor surge [33].

2) *Pressure ratio*: Unlike Positive displacement compressors, such as screw and scroll types, centrifugal compressor can not work on a constant pressure ratio if it is not appropriately controlled. In

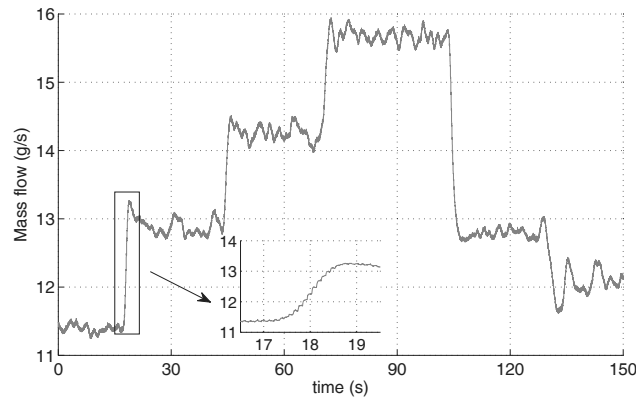


Fig. 11. Measured mass flow.

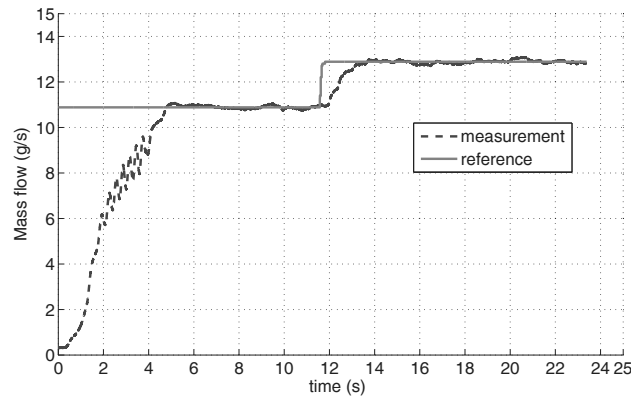


Fig. 12. Mass flow response controlled by PI controller (from [33]).

fuel cell, higher pressure can lead to higher stack output voltage. Moreover, stacks designed for high working pressures are smaller and consequently less expensive. However, higher pressure also implies higher power consumption on the compressor. The nominal compression ratio is determined depending on the fuel cell stack and practical cases, on which maximum efficiency is produced. It should be noticed that a greater pressure ripple would damage (perforate) the membrane. In automotive applications, no pressure ripple greater than 100–200 mbars is allowed [1].

Under the imposed current, dynamic characteristics of inlet manifold pressure and the fuel cell output voltage are shown in Fig. 13 and Fig. 14 respectively, which show that the pressure is maintained around 1.4 bar with pressure ripple less than 50 mbars under steady state. Pressure deviations at 20 s, 45 s, 70 s,

100 s, 130 s are due to sudden changes of mass flow, thereby sudden deviations of the output voltage. Fig. 15 exhibits the dynamic behavior of the net power generated by the fuel cell. Fig. 16 gives the compressor rotational speed during the operation. In the interval of 70s-100s, the compressor reached its maximum speed, i.e. 260,000 rpm.

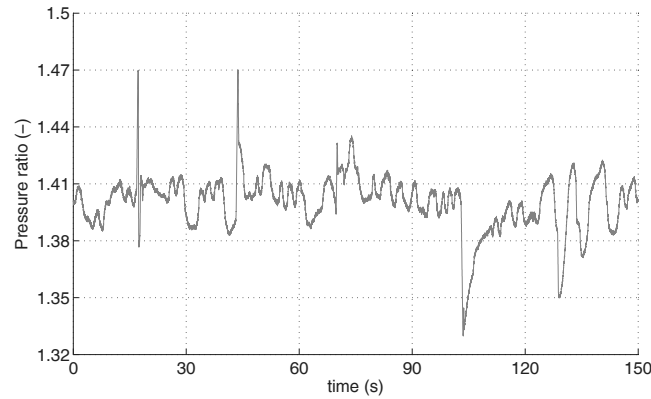


Fig. 13. Measured supplied pressure ratio.

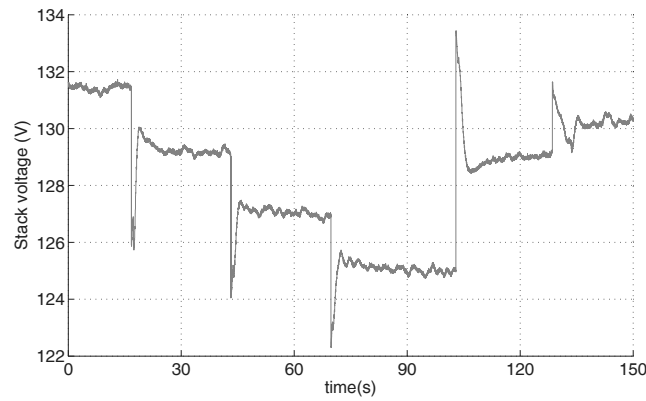


Fig. 14. Stack output voltage.

Finally, dynamics of the control variables (motor torque and control valve angle) during the operation are presented in Fig. 17.

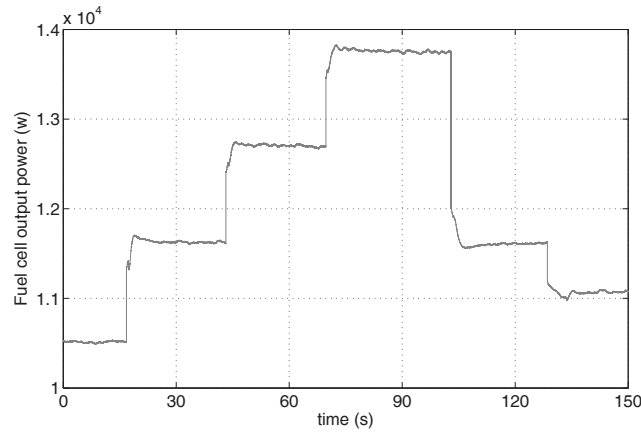


Fig. 15. Fuel cell output power.

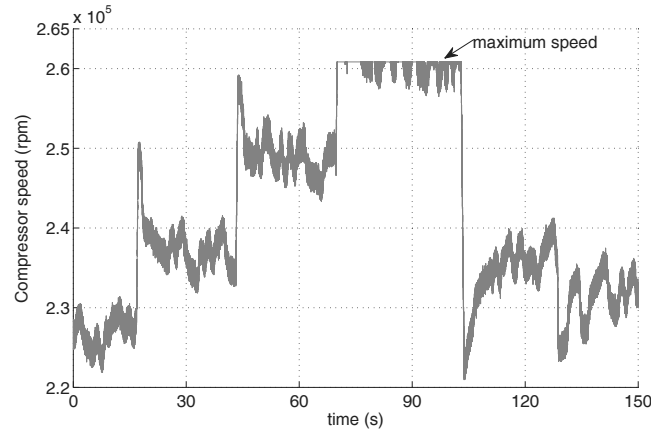
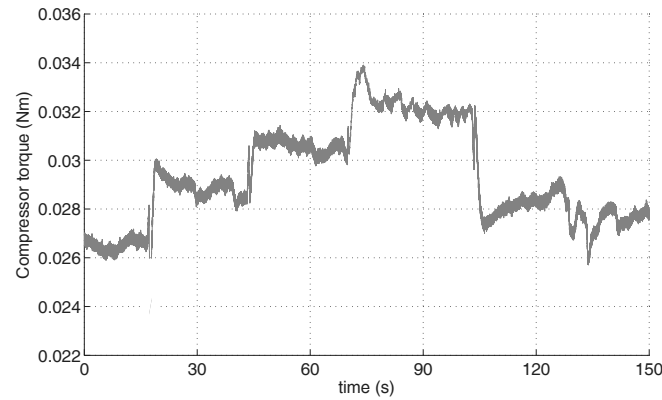


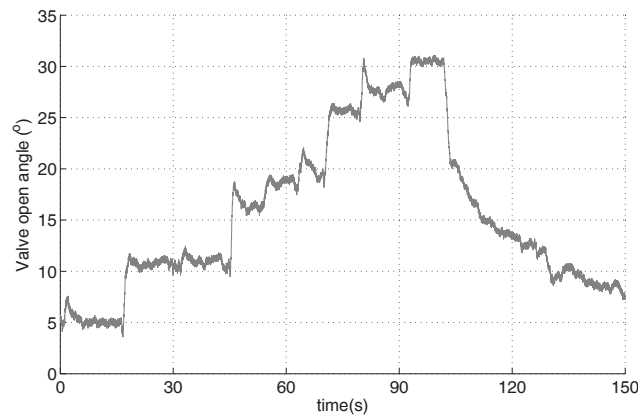
Fig. 16. Compressor rotational speed.

## VII. CONCLUSION

This paper has presented a technological solution for the air management of fuel cell for automotive applications. An ultra high speed centrifugal compressor has been adopted for the reasons of compactness, high efficiency and low noise. A neural network model of the compressor has been developed based on the measured compressor map. Decentralized sliding model control strategy based on the twisting and super twisting algorithm has been proposed for the control of compressor mass flow rate and pressure ratio respectively according to the load demand. The stability and convergency of the controller are achieved by appropriately configuring the control parameters. The experimental validation of the control system



(a) Motor torque



(b) Control valve open angle

Fig. 17. The dynamic of the control variables during the cycle.

is performed on a hardware-in-the-loop platform. Dynamic characteristics of the performance parameters (oxygen excess ratio, mass flow, pressure, etc) have been tested. The results have shown the rapid response and stability of the designed system. In our knowledge, the proposed compressor and associated control are original and show more interests for automotive applications compared with previous literatures.

Further research will focus on the low mass flow rate control, which involve compressor surge control. A reference limiter has been proposed in [43] for the surge control in view of easy application. The convergence and stability of that limiter applied to this controller also need to be validated theoretically and experimentally.

## APPENDIX

TABLE III  
COMPRESSOR NEURAL NETWORK MODEL PARAMETERS

First hidden layer parameters								
$a_1 = 5.5584 * 10^{-5}$	$b_1 = -19.3352$	$c_1 = 13.9266$						
$a_2 = 8.1815 * 10^{-6}$	$b_2 = -10.38621$	$c_2 = 13.7624$						
$a_3 = 3.3295 * 10^{-5}$	$b_3 = -7.4481$	$c_3 = 2.6424$						
$a_4 = 9.7400 * 10^{-3}$	$b_4 = 18.6128$	$c_4 = -21.3957$						
$a_5 = -1.8965 * 10^{-3}$	$b_5 = -14.5898$	$c_5 = 16.1518$						
$a_6 = -1.5174 * 10^{-5}$	$b_6 = 6.9198$	$c_6 = -6.8043$						
$a_7 = 3.1838 * 10^{-5}$	$b_7 = 15.1593$	$c_7 = -26.5838$						
$a_8 = 2.0906 * 10^{-5}$	$b_8 = 7.3221$	$c_8 = 14.2375$						
$a_9 = 9.3429 * 10^{-4}$	$b_9 = -11.9357$	$c_9 = 9.5622$						
$a_{10} = 3.5940 * 10^{-6}$	$b_{10} = -16.1595$	$c_{10} = 17.5984$						
$a_{11} = 2.5981 * 10^{-5}$	$b_{11} = -3.2896$	$c_{11} = -0.5859$						
$a_{12} = -1.2737 * 10^{-4}$	$b_{12} = 9.7639$	$c_{12} = 19.3709$						
$a_{13} = -0.04657621$	$b_{13} = -15.1535$	$c_{13} = 19.7660$						
$a_{14} = -9.3907 * 10^{-4}$	$b_{14} = -14.5847$	$c_{14} = 19.0636$						
$a_{15} = 3.4333 * 10^{-4}$	$b_{15} = -3.2114$	$c_{15} = 1.5582$						
Second hidden layer parameters								
$e_1 = 0.6623$	$e_2 = 0.9705$	$e_3 = -0.2235$	$e_4 = -0.6251$	$e_5 = 0.6221$	$e_6 = 0.04278$	$e_7 = 0.04836$	$e_8 = 0.3967$	
$l_{1,1} = 0.581$	$l_{1,2} = 0.519$	$l_{1,3} = -0.193$	$l_{1,4} = -0.711$	$l_{1,5} = -0.501$	$l_{1,6} = 0.092$	$l_{1,7} = 0.785$	$l_{1,8} = -0.432$	
$l_{2,1} = 0.442$	$l_{2,2} = -0.016$	$l_{2,3} = -0.773$	$l_{2,4} = 0.658$	$l_{2,5} = -1.097$	$l_{2,6} = -1.23$	$l_{2,7} = 1.633$	$l_{2,8} = -0.332$	
$l_{3,1} = 0.082$	$l_{3,2} = -0.622$	$l_{3,3} = -0.309$	$l_{3,4} = 0.406$	$l_{3,5} = -0.179$	$l_{3,6} = -0.816$	$l_{3,7} = 0.573$	$l_{3,8} = 0.071$	
$l_{4,1} = -0.594$	$l_{4,2} = -0.480$	$l_{4,3} = 0.490$	$l_{4,4} = 0.865$	$l_{4,5} = 0.122$	$l_{4,6} = 0.069$	$l_{4,7} = 1.003$	$l_{4,8} = 0.704$	
$l_{5,1} = 0.395$	$l_{5,2} = 1.232$	$l_{5,3} = -0.349$	$l_{5,4} = -0.320$	$l_{5,5} = 0.209$	$l_{5,6} = 0.034$	$l_{5,7} = -1.479$	$l_{5,8} = 0.737$	
$l_{6,1} = 1.619$	$l_{6,2} = -2.278$	$l_{6,3} = -3.026$	$l_{6,4} = 1.725$	$l_{6,5} = -1.890$	$l_{6,6} = -3.351$	$l_{6,7} = 2.468$	$l_{6,8} = -0.410$	
$l_{7,1} = 0.367$	$l_{7,2} = 1.061$	$l_{7,3} = -0.794$	$l_{7,4} = 0.142$	$l_{7,5} = 0.475$	$l_{7,6} = -0.298$	$l_{7,7} = 0.417$	$l_{7,8} = -0.446$	
$l_{8,1} = -0.968$	$l_{8,2} = -0.649$	$l_{8,3} = 0.941$	$l_{8,4} = 0.377$	$l_{8,5} = 0.750$	$l_{8,6} = 0.670$	$l_{8,7} = 0.210$	$l_{8,8} = -1.126$	
$l_{9,1} = -0.649$	$l_{9,2} = -0.138$	$l_{9,3} = 0.308$	$l_{9,4} = 0.355$	$l_{9,5} = -0.166$	$l_{9,6} = 0.482$	$l_{9,7} = -1.340$	$l_{9,8} = -0.647$	
$l_{10,1} = 0.413$	$l_{10,2} = -0.370$	$l_{10,3} = 0.959$	$l_{10,4} = -0.531$	$l_{10,5} = 0.521$	$l_{10,6} = -0.588$	$l_{10,7} = 0.108$	$l_{10,8} = -0.080$	
$l_{11,1} = 0.806$	$l_{11,2} = -0.120$	$l_{11,3} = 0.245$	$l_{11,4} = -0.835$	$l_{11,5} = 1.195$	$l_{11,6} = 0.546$	$l_{11,7} = -1.495$	$l_{11,8} = 0.195$	
$l_{12,1} = -0.312$	$l_{12,2} = -0.057$	$l_{12,3} = 0.846$	$l_{12,4} = 0.450$	$l_{12,5} = -0.313$	$l_{12,6} = 0.409$	$l_{12,7} = -0.573$	$l_{12,8} = -0.816$	
$l_{13,1} = 0.110$	$l_{13,2} = 0.936$	$l_{13,3} = -0.660$	$l_{13,4} = 0.607$	$l_{13,5} = 0.284$	$l_{13,6} = -0.063$	$l_{13,7} = -0.736$	$l_{13,8} = -0.337$	
$l_{14,1} = -0.179$	$l_{14,2} = 0.243$	$l_{14,3} = 0.020$	$l_{14,4} = 0.464$	$l_{14,5} = 0.943$	$l_{14,6} = 0.839$	$l_{14,7} = -0.574$	$l_{14,8} = 0.078$	
$l_{15,1} = 0.019$	$l_{15,2} = -0.563$	$l_{15,3} = 0.124$	$l_{15,4} = -0.589$	$l_{15,5} = 0.261$	$l_{15,6} = 0.973$	$l_{15,7} = -0.302$	$l_{15,8} = -0.902$	
Output layer parameters								
$w_1 = -1.1852$	$w_2 = 2.0229$	$w_3 = 2.8164$	$w_4 = -1.7167$	$w_5 = 2.3587$	$w_6 = 3.4640$	$w_7 = -3.4376$	$w_8 = 0.1238$	$d = 0.5220$



## REFERENCES

- [1] B. Blunier and A. Miraoui, "Proton exchange membrane fuel cell air management in automotive applications," *Journal of Fuel Cell Science and Technology*, vol. 7, no. 041007, p. 041007, 2010.
- [2] A. Ravey, N. Watrin, B. Blunier, D. Bouquain, and A. Miraoui, "Energy-source-sizing methodology for hybrid fuel cell vehicles based on statistical description of driving cycles," *Vehicular Technology, IEEE Transactions on*, vol. 60, no. 9, pp. 4164–4174, 2011.
- [3] A. Ravey, B. Blunier, and A. Miraoui, "Control strategies for fuel-cell-based hybrid electric vehicles: From offline to online and experimental results," *Vehicular Technology, IEEE Transactions on*, vol. 61, no. 6, pp. 2452–2457, 2012.
- [4] J. Jespersen, E. Schaltz, and S. Kær, "Electrochemical characterization of a polybenzimidazole-based high temperature proton exchange membrane unit cell," *Journal of Power Sources*, vol. 191, no. 2, pp. 289–296, 2009.
- [5] H. Jensen and S. Kær, "Boundary model-based reference control of blower cooled high temperature polymer electrolyte membrane fuel cells," *International Journal of Hydrogen Energy*, vol. 36, no. 8, pp. 5030–5037, 2011.
- [6] T. Berning, M. Odgaard, and S. Kær, "A study of multi-phase flow through the cathode side of an interdigitated flow field using a multi-fluid model," *Journal of Power Sources*, vol. 195, no. 15, pp. 4842–4852, 2010.
- [7] S. Andreasen and S. Kær, "Modelling and evaluation of heating strategies for high temperature polymer electrolyte membrane fuel cell stacks," *International Journal of Hydrogen Energy*, vol. 33, no. 17, pp. 4655–4664, 2008.
- [8] L. Xu, F. Yang, J. Li, M. Ouyang, and J. Hua, "Real time optimal energy management strategy targeting at minimizing daily operation cost for a plug-in fuel cell city bus," *International Journal of Hydrogen Energy*, 2012.
- [9] J. Gonder and T. Markel, "Energy management strategies for plug-in hybrid electric vehicles," in *SAE world congress*, 2007, pp. 1–5.
- [10] L. Xu, J. Li, J. Hua, X. Li, and M. Ouyang, "Adaptive supervisory control strategy of a fuel cell/battery-powered city bus," *Journal of Power Sources*, vol. 194, no. 1, pp. 360–368, 2009.
- [11] A. Fadel and B. Zhou, "An experimental and analytical comparison study of power management methodologies of fuel cell–battery hybrid vehicles," *Journal of Power Sources*, vol. 196, no. 6, pp. 3271–3279, 2011.
- [12] L. Xu, J. Li, J. Hua, X. Li, and M. Ouyang, "Optimal vehicle control strategy of a fuel cell/battery hybrid city bus," *International Journal of Hydrogen Energy*, vol. 34, no. 17, pp. 7323–7333, 2009.
- [13] A. Vahidi, A. Stefanopoulou, and H. Peng, "Model predictive control for starvation prevention in a hybrid fuel cell system," in *Proc. American Control Conf the 2004*, vol. 1, pp. 834–839.
- [14] A. Vahidi, A. Stefanopoulou, and H. Peng, "Current management in a hybrid fuel cell power system: A model-predictive control approach," vol. 14, no. 6, pp. 1047–1057, 2006.
- [15] B. Blunier, M. Pucci, G. Cirrincione, M. Cirrincione, and A. Miraoui, "A scroll compressor with a high-performance sensorless induction motor drive for the air management of a pemfc system for automotive applications," *Vehicular Technology, IEEE Transactions on*, vol. 57, no. 6, pp. 3413–3427, 2008.
- [16] B. Blunier, G. Cirrincione, Y. Hervé, and A. Miraoui, "A new analytical and dynamical model of a scroll compressor with experimental validation," *International Journal of Refrigeration*, vol. 32, no. 5, pp. 874–891, 2009.
- [17] J. Cunningham, M. Hoffman, and D. Friedman, "A comparison of high-pressure and low-pressure operation of pem fuel cell systems," 2001.
- [18] B. Blunier and A. Miraoui, "Air management in pem fuel cells: State-of-the-art and perspectives," in *Proc. Int. Aegean Conf. Electrical Machines and Power Electronics ACEMP '07*, 2007, pp. 245–254.

- [19] C. Kunusch, P. Puleston, M. Mayosky, and J. Riera, "Sliding mode strategy for pem fuel cells stacks breathing control using a super-twisting algorithm," *Control Systems Technology, IEEE Transactions on*, vol. 17, no. 1, pp. 167–174, 2009.
- [20] W. Garcia-Gabin, F. Dorado, and C. Bordons, "Real-time implementation of a sliding mode controller for air supply on a pem fuel cell," *Journal of process control*, vol. 20, no. 3, pp. 325–336, 2010.
- [21] R. Talj, D. Hissel, R. Ortega, M. Becherif, and M. Hilaret, "Experimental validation of a pem fuel-cell reduced-order model and a moto-compressor higher order sliding-mode control," *Industrial Electronics, IEEE Transactions on*, vol. 57, no. 6, pp. 1906–1913, 2010.
- [22] I. Matraji, S. Laghrouche, and M. Wack, "Cascade control of the moto-compressor of a pem fuel cell via second order sliding mode," in *Decision and Control and European Control Conference (CDC-ECC), 2011 50th IEEE Conference on*. IEEE, 2011, pp. 633–638.
- [23] J. Larminie, A. Dicks, and K. (Firm)., "Fuel cell systems explained," 2003.
- [24] D. Krähenbühl, C. Zwyssig, H. Weser, and J. Kolar, "A miniature 500 000-r/min electrically driven turbocompressor," *Industry Applications, IEEE Transactions on*, vol. 46, no. 6, pp. 2459–2466, 2010.
- [25] D. Zhao, D. Krähenbühl, B. Blunier, C. Zwyssig, M. Dou, and A. Miraoui, "Design and control of an ultra high speed centrifugal compressor for the air management of fuel cell," in *Transportation Electrification Conference Exop.* IEEE, 2012.
- [26] J. Pukrushpan, A. Stefanopoulou, and H. Peng, "Control of fuel cell breathing," *Control Systems Magazine, IEEE*, vol. 24, no. 2, pp. 30–46, 2004.
- [27] J. Gruber, C. Bordons, and A. Oliva, "Nonlinear mpc for the airflow in a pem fuel cell using a volterra series model," *Control Engineering Practice*, vol. 20, no. 2, pp. 205 – 217, 2012.
- [28] A. Arce, A. del Real, C. Bordons, and D. Ramírez, "Real-time implementation of a constrained mpc for efficient airflow control in a pem fuel cell," *Industrial Electronics, IEEE Transactions on*, vol. 57, no. 6, pp. 1892–1905, 2010.
- [29] Y. Chang and S. Moura, "Air flow control in fuel cell systems: An extremum seeking approach," in *American Control Conference, 2009. ACC'09.* IEEE, 2009, pp. 1052–1059.
- [30] A. Arce, D. Ramirez, A. del Real, and C. Bordons, "Constrained explicit predictive control strategies for pem fuel cell systems," in *Decision and Control, 2007 46th IEEE Conference on.* IEEE, 2007, pp. 6088–6093.
- [31] M. Nored, K. Brun, and R. Kurz, "Development of a guideline for the design of surge control systems," *ASME Turbo Expo, Berlin, June*, pp. 9–13, 2008.
- [32] J. Gravdahl and O. Egeland, "Compressor surge control using a close-coupled valve and backstepping," in *American Control Conference, 1997. Proceedings of the 1997*, vol. 2. IEEE, 1997, pp. 982–986.
- [33] D. Zhao, M. Dou, B. Blunier, and A. Miraoui, "Control of an ultra high speed centrifugal compressor for the air management of fuel cell systems," in *Industry Applications Society Annual Meeting (IAS), 2012 IEEE.* IEEE, 2012, pp. 1–8.
- [34] J. Pukrushpan, "Modeling and control of fuel cell systems and fuel processors," *Amercia: The University of Michigan*, 2003.
- [35] F. Gao, D. Chrenko, B. Blunier, D. Bouquain, and A. Miraoui, "Multi-rates fuel cell emulation with spatial reduced real-time fuel cell modelling," in *Industry Applications, IEEE Transactions on.* IEEE, 2011, pp. 1–8.
- [36] F. Gao, B. Blunier, M. Simoes, and A. Miraoui, "Pem fuel cell stack modeling for real-time emulation in hardware-in-the-loop applications," *Energy Conversion, IEEE Transactions on*, no. 99, pp. 1–11, 2011.
- [37] F. Gao, B. Blunier, A. Miraoui, and A. El-Moudni, "Proton exchange membrane fuel cell multi-physical dynamics and stack spatial non-homogeneity analyses," *Journal of Power Sources*, vol. 195, no. 22, pp. 7609–7626, 2010.

- [38] F. Gao, B. Blunier, A. Miraoui, and A. El Moudni, "A multiphysic dynamic 1-d model of a proton-exchange-membrane fuel-cell stack for real-time simulation," *Industrial Electronics, IEEE Transactions on*, vol. 57, no. 6, pp. 1853–1864, 2010.
- [39] D. Chrenko, F. Gao, B. Blunier, D. Bouquain, and A. Miraoui, "Methanol fuel processor and pem fuel cell modeling for mobile application," *International Journal of Hydrogen Energy*, vol. 35, no. 13, pp. 6863–6871, 2010.
- [40] T. Nguyen and R. White, "A water and heat management model for proton-exchange-membrane fuel cells," *Journal of the Electrochemical Society*, vol. 140, no. 8, pp. 2178–2186, 1993.
- [41] A. Vahidi, I. Kolmanovsky, and A. Stefanopoulou, "Constraint management in fuel cells: A fast reference governor approach," in *American Control Conference, 2005. Proceedings of the 2005.* IEEE, 2005, pp. 3865–3870.
- [42] M. Grujicic, K. Chittajallu, E. Law, and J. Pukrushpan, "Model-based control strategies in the dynamic interaction of air supply and fuel cell," *Proceedings of the Institution of Mechanical Engineers, Part A: Journal of Power and Energy*, vol. 218, no. 7, pp. 487–499, 2004.
- [43] D. Zhao, B. Blunier, M. Dou, and A. Miraoui, "Control of an ultra high speed centrifugal compressor for the air management of fuel cell systems," in *Industry Application Society Annual Meeting (accepted for publication).* IEEE, 2012.
- [44] L. Fridman and A. Levant, "Higher order sliding modes," *Sliding mode control in engineering*, vol. 11, pp. 53–102, 2002.
- [45] A. Levant, "Robust exact differentiation via sliding mode technique," *Automatica*, vol. 34, no. 3, pp. 379–384, 1998.